[Supporting Information] Ordering Dynamics of Blue Phases: Kinetic Stabilization of Amorphous Networks

Oliver Henrich [*] , **Kevin Stratford** [†], **Davide Marenduzzo** [*] , **and Michael E. Cates** [*]

[*]SUPA, School of Physics and Astronomy, University of Edinburgh, Mayfield Road, Edinburgh EH9 3JZ, UK, and [†]EPCC, University of Edinburgh, Mayfield Road, Edinburgh EH9 3JZ, UK

Submitted to Proceedings of the National Academy of Sciences of the United States of America

Supporting Text S1

Here we provide further information on the free energy functional and the control parameters τ, κ (section 1); on the equations of motion (section 2); on the conversion of simulation parameters to physical units (section 3); on the introduction of thermal noise (section 4); on the parameter values for our quenches (section 5); and on the end-state free energies in comparison with various stable and metastable phases (section 6).

1. Free energy functional, chirality and reduced temperature. The thermodynamics of cholesteric blue phases can be described via a Landau-de Gennes free energy functional $\mathcal{F}$, which in turn is an integral over space of a free energy density f,

$$\mathcal{F}[\mathbf{Q}] \;=\; \int d^3\mathbf{r} f(\mathbf{Q}(\mathbf{r})). \qquad [1]$$

The free energy density $f = f(\mathbf{Q})$ may be expanded in powers of the order parameter $\mathbf{Q}$ and its gradients; $\mathbf{Q}$ is a traceless and symmetric tensor. The largest eigenvalue q and corresponding eigendirection ($\mathbf{n}$) respectively describe the local strength and major orientation axis of molecular order. The $\mathbf{Q}$ tensor theory, rather than a theory based solely on the director field $\mathbf{n}(\mathbf{r})$, allows treatment of disclinations (defect lines) in whose cores $\mathbf{n}$ is undefined; in blue phases, disclinations organise into regular or amorphous networks.

The free energy density we use, following [7], is:

$$\begin{aligned} f(\mathbf{Q}) \;&=\; \frac{A_0}{2}\left(1-\frac{\gamma}{3}\right)Q_{\alpha\beta}^2 \\ &-\; \frac{A_0\gamma}{3}Q_{\alpha\beta}Q_{\beta\gamma}Q_{\gamma\alpha} + \frac{A_0\gamma}{4}(Q_{\alpha\beta}^2)^2 \\ &+\; \frac{K}{2}(\varepsilon_{\alpha\gamma\delta}\partial_\gamma Q_{\delta\beta} + 2q_0 Q_{\alpha\beta})^2 + \frac{K}{2}(\partial_\beta Q_{\alpha\beta})^2 \quad [2] \end{aligned}$$

Here repeated indices are summed over and $Q_{\alpha\beta}^2$ stands for $Q_{\alpha\beta}Q_{\alpha\beta}$ etc.. The first three terms are a bulk free energy density whose overall scale is set by A_0 (discussed further below); γ is a control parameter, related to reduced temperature. Varying the latter in the absence of chiral terms ($q_0 = 0$) gives an isotropic-nematic transition at $\gamma = 2.7$ with a mean-field spinodal instability at $\gamma = 3$.

The rest of the free energy in Eq.2 describes distortions of the order parameter field. As is conventional [7, 5] we assume that splay, bend and twist deformations of the director are equally costly; K is then the one elastic constant that remains. The parameter q_0 is related via $q_0 = 2\pi/p_0$ to the pitch length, p_0, describing one full turn of the director in the cholesteric phase. In BPs one observes that the pitch length (still defined locally by the spatial rotation rate of $\mathbf{n}$) slightly increases on entering the BP from the cholesteric phase. To account for this, a 'redshift' factor r is introduced [9] whose variation effectively allows free adjustment of the BP lattice parameter, $\Lambda \to \Lambda/r$. To avoid changing the size of the simulation box, redshifting is performed in practice by an equivalent rescaling of the pitch parameter and elastic constant, $q_0 \to q_0/r$ and $K \to K\,r^2$. In simulations aimed solely at free energy minimization, it is legitimate to make r a dynamic parameter and update it on the fly to achieve this [9]. We do not allow this during our domain growth runs, but do relax r at the end of selected runs as part of our free energy comparison (see Section 6).

The phase diagram of blue phases (if thermal fluctuations can be neglected [10]) depends on just two dimensionless numbers, which are commonly referred to as κ, the *chirality*, and τ, the *reduced temperature* [7]. In terms of the above parameters, these are:

$$\tau \;=\; \frac{27(1-\gamma/3)}{\gamma} \qquad [3]$$

$$\kappa \;=\; \sqrt{\frac{108\;K\,q_0^2}{A_0\,\gamma}}. \qquad [4]$$

If the free energy density Eq.2 is made dimensionless, τ appears as prefactor of the term quadratic in $\mathbf{Q}$, whereas κ quantifies the ratio between bulk and gradient free energy terms.

2. Equations of motion. A framework for the dynamics of liquid crystals is provided by the Beris-Edwards model [4], in which the time evolution of the tensor order parameter obeys

$$(\partial_t + u_\alpha\partial_\alpha)\,\mathbf{Q} - \mathbf{S}(\mathbf{W},\mathbf{Q}) = \Gamma\mathbf{H} + \boldsymbol{\zeta} \qquad [5]$$

where $\boldsymbol{\zeta}$ is a noise term discussed in section 4. In the absence of flow, Eq.5 describes relaxation towards equilibrium, with a rotational diffusion constant Γ, driven by the molecular field $\mathbf{H}$. The latter is given by [4]

$$\mathbf{H} = -\frac{\delta\mathcal{F}}{\delta\mathbf{Q}} + \frac{\mathbf{I}}{3}\mathrm{Tr}\left(\frac{\delta\mathcal{F}}{\delta\mathbf{Q}}\right). \qquad [6]$$

The tensor $\mathbf{S}$ in Eq.5 couples the order parameter to the symmetric and antisymmetric parts of the velocity gradient tensor

Reserved for Publication Footnotes

$W_{\alpha\beta} \equiv \partial_\beta u_\alpha$, defined as

$$\mathbf{A} = (\mathbf{W} + \mathbf{W}^T)/2; \;\; \mathbf{\Omega} = (\mathbf{W} - \mathbf{W}^T)/2. \qquad [7]$$

This coupling term reads explicitly

$$\begin{aligned} \mathbf{S}(\mathbf{W}, \mathbf{Q}) &= (\xi\mathbf{A} + \mathbf{\Omega})(\mathbf{Q} + \frac{\mathbf{I}}{3}) + (\mathbf{Q} + \frac{\mathbf{I}}{3})(\xi\mathbf{A} - \mathbf{\Omega}) \\ &- 2\xi(\mathbf{Q} + \frac{\mathbf{I}}{3})\mathrm{Tr}(\mathbf{Q}\mathbf{W}). \end{aligned} \qquad [8]$$

Here ξ is a material-dependent 'tumbling parameter' that controls the relative importance of rotational and elongational flow for molecular alignment. We choose $\xi = 0.7$, within the 'flow aligning' regime for which molecules align at a fixed angle (the Leslie angle) to the flow direction in weak simple shear [5]. (For 'flow tumbling' materials, the director instead rotates continuously [5, 4].)

The momentum evolution obeys a Navier-Stokes equation driven by the divergence of a stress tensor $\mathbf{\Sigma}$:

$$\rho\, \partial_t u_\alpha + \rho\, u_\beta \partial_\beta u_\alpha = \partial_\beta \Sigma_{\alpha\beta} \qquad [9]$$

This pressure tensor is in general asymmetric and includes both viscous and thermodynamic components

$$\begin{aligned} \Sigma_{\alpha\beta} &= -P_0\delta_{\alpha\beta} + \eta\{\partial_\alpha u_\beta + \partial_\beta u_\alpha\} \\ &- \xi H_{\alpha\gamma}\left(Q_{\gamma\beta} + \frac{\delta_{\gamma\beta}}{3}\right) - \xi\left(Q_{\alpha\gamma} + \frac{1}{3}\delta_{\alpha\gamma}\right)H_{\gamma\beta} \\ &+ 2\xi\left(Q_{\alpha\beta} + \frac{1}{3}\delta_{\alpha\beta}\right)Q_{\gamma\nu}H_{\gamma\nu} - \partial_\alpha Q_{\gamma\nu}\frac{\delta\mathcal{F}}{\delta\partial_\beta Q_{\gamma\nu}} \\ &+ Q_{\alpha\gamma}H_{\gamma\beta} - H_{\alpha\gamma}Q_{\gamma\beta} \end{aligned} \qquad [10]$$

Note that within the lattice Boltzmann flow solver, the isotropic pressure and viscous terms are managed directly by the solver (as in a simple Newtonian fluid, of viscosity η) whereas the divergence of the remaining terms is treated as a local force density on that fluid.

3. Parameter mapping to physical units. Here we describe how simulation parameters are related to physical quantities in real BP materials. In order to get from simulation to physical units, we need to calibrate scales of mass, length, and time (or equivalently length, energy and time). We follow a methodology similar to that of [8].

First we define a set of LB units (LBU) in which the lattice parameter ℓ, the time step Δt, and a reference fluid mass density ρ_0 are all set to unity. This is the set of units in which our algorithm is actually written. The first two of these parameters directly connect to observables in the simulations and we show below how to map these onto experiments. The fluid density, however, enters differently. So long as fluid inertia remains negligible (low Reynolds number, $\mathrm{Re} = \rho V\Lambda/\eta$, where V, Λ are typical length scales and velocities of any flow) the physics observed will not depend on the actual mass density ρ of either the physical or the simulated system. Since LB uses inertia to update the fluid velocities, it improves efficiency to use a density that causes Re to be several orders of magnitude larger than in experiments; so long as Re remains small (say, $\mathrm{Re} < 0.1$), no harm is done [11]. Such parameter steering is helped by allowing $\rho \neq \rho_0$ within the code.

We now turn to the calibrations of length, energy and time. The length scale calibration is straightforward, and fixed by the cholesteric pitch p_0, which is typically in the 100-500 nm range [7]. More precisely, in our simulations we set the unit cell of BPI/II to be 16 LBU; this gives good resolution without wasting resource. Therefore the LBU length unit (one lattice site) corresponds to, say, 10nm in physical space.

To get an energy scale, we use the measurements cited in Appendix D of [7], which suggest

$$\frac{a}{b^2} = \frac{27}{2A_0\gamma} \sim 2 - 5 \times 10^{-6}\mathrm{J}^{-1}\,\mathrm{m}^3. \qquad [11]$$

Here a, b are parameters defined in [7], and the required ratio is expressed in terms of our chosen parameters (whose comparison with [7] shows that $b\sqrt{6} = A_0\gamma/3$ and $a = A_0\gamma/4$). From this relation, given that $\gamma \simeq 3$, we obtain that $A_0 \simeq 10^6$ Pa. On the other hand, our simulations use a value of $A_0 \simeq 0.01$ LBU. This requires that the LB unit of stress is about 10^8 Pa in SI units. We next use this to calibrate the LB time unit and then crosscheck that the resulting fluid density gives acceptable Reynolds numbers.

For the timescale calibration we use the following formula [5, 8] which relates the so-called 'rotational viscosity' γ_1 (defined by the relaxation equation $\gamma_1\partial\mathbf{n}/\partial t = -\delta F/\delta\mathbf{n}$) for the director field in a well-aligned nematic, to the ordering strength q and the order parameter mobility Γ:

$$\gamma_1 = \frac{2q^2}{\Gamma}\,. \qquad [12]$$

In our simulations, we choose $\Gamma = 0.3$ and also select the thermodynamic parameters to give $q \simeq 0.3$. Therefore $\gamma_1 \simeq 0.6$ LBU. For real materials, γ_1 lies usually in range $10^{-2} - 10^{-1}$ Pa s [5]; we choose for definiteness $\gamma_1 = 0.06$ Pa s $= 0.6$ LBU. Given the previous result for stress, this requires that the LB time unit (one algorithmic timestep) equates to 10^{-9} s.

Note that in our simulations we use a fluid viscosity $\eta \simeq 1 - 2$ LBU $= 0.1 - 0.2$ Pa s (using the parameter mapping just established). This is sensible (if somewhat low) for a molecular nematogen in the isotropic phase. (The effective viscosity in ordered phases is of course higher, but the coupling to the order parameter handles this.) Similarly, we adopt elastic constant values $K \simeq 0.01$ LBU $= 10^{-10}$ N, corresponding to a Frank elastic constant $K/2$ of 50 pN which is again sensible [5].

Finally, we need to cross-check the fluid density. We have 1 kg m^{-3} = 1 Pa s^2 m^{-2} = $10^{-8+18-16}$ LBU = 10^{-6} LBU. Thus the reference density ρ_0 equates to a fluid density $\rho = 10^6$ kg m^{-3}, roughly a thousand times larger than experimental values. As explained previously, however, this makes no difference so long as the Reynolds number $\mathrm{Re} = \rho V\Lambda/\eta$ remains small enough. This dimensionless number can be evaluated directly in lattice units. We have ρ and η of order unity, and set $\Lambda \sim 16$ (a BP unit cell). Observing that typical velocities arising in our simulations are around 10^{-5} LBU we get Re $\lesssim 10^{-3}$. Even allowing for higher peak velocities and larger Λ in some materials, this is safely small [11].

To summarize the above, our simulations faithfully represent experimentally realisable BP-forming materials, subject to the interpretation of the LB units for length, time, and energy density are close to 10 nm, 1 ns, and 100 MPa respectively.

4. Adding noise. With these choices, the typical difference in free energy density between say BPI and BPII is $10^{-6} - 10^{-5}$ LBU (see Table S2) or about $100 - 1000$ Pa. Even for a rather small BP lattice constant of 160 nm, this corresponds to a free energy difference per unit cell of $100 - 1000\ k_BT$, much larger than any thermal energy. Such unit-cell level differences represent a reasonable estimate of the barrier to topological reconnections within an evolving BP structure, and appear to preclude any significant role for thermal noise in the domain growth process. Nonetheless it has been argued theoretically

[10] that entropy plays an important role in BP thermodynamics and presumably also therefore, domain growth. (This certainly becomes more likely for atypically small A_0 and/or small unit cells.) We therefore repeated selected simulations with thermal noise present.

We choose to add noise to the order parameter sector only, via the $\zeta_{\alpha\beta}$ term in Eq.5. In principle, noise can also be added to the fluid mechanical sector [12]; this will create an additional conserved diffusion of the order parameter (a kind of Brownian motion) which should however be negligible, at least at large length scales, compared to the local nonconservative relaxation embodied in Eq.5. The fluctuation-dissipation theorem then fixes the variance of the noise in Eq.5 as

$$\langle \zeta_{\alpha\beta}(\mathbf{r},t)\zeta_{\gamma\delta}(\mathbf{r}',t')\rangle = 2k_BT\Gamma P_{\alpha\beta\gamma\delta}\delta(\mathbf{r}-\mathbf{r}')\delta(t-t'). \quad \textbf{[13]}$$

Here $\mathbf{P}$ is a tensor that projects the order parameter into independent components (respecting its symmetry and tracelessness) and allows only diagonal correlations in that space.

By using the parameter mapping detailed above, we can find the value of $k_BT = 4\times10^{-21}$J in simulation units as 4×10^{-5} LBU. However, to allow for variation in material parameters, such as the BP unit cell size, we have studied a range of noise temperatures in the range 10^{-6}–10^{-4} LBU. At the upper end of this range we can observe vibrant thermal fluctuations of the disclination network, associated with some shifting of phase boundaries. This merits further study in view of the claims of [10] that fluctuations can signigicantly alter the equilibrium physics of blue phases, although a full exploration of such effects lie beyond the scope of the current work. However, in terms of domain growth dynamics, we have found the main effects of adding modest amounts of thermal noise to be quantitative rather than qualitative. (Here 'modest' means $k_BT \leq 10^{-5}$ LBU, as might be relevant to BPs with lattice parameters $\geq$ 300 nm rather than the 160nm value used in the parameter mapping in section 3.) An exception was already discussed in relation to Fig.S1, which shows that quite low noise levels can disrupt the orderly but aperiodic growth that would otherwise arise from a rod-like nucleus.

5. Quench details. Quenches were performed as described in the Methods section of the main text. Supporting Table S1 specifies the complete simulation parameters (all in LBU) for each of the runs presented in Figures 2-5 of the main text and Figures S1-S2.

6. Free energy comparisons. Supporting Table S2 compares the free energy densities of three crystalline blue phases (BPI, BPII, O5) with the cholesteric phase and the end-state amorphous networks for the final τ, κ values appropriate to all runs reported in Figs.2-5 and Figs.S1,S2. (The noise-free isotropic phase has free energy density zero in all cases.) Note that O5, as long predicted theoretically [7], becomes the most stable ordered phase at high chirality. However this phase is not seen experimentally and its relative stability might be a consequence of the one elastic constant approximation or some other shortcoming of the free energy, Eq.2.

For end-state amorphs nucleated within an isotropic phase, two free energy values are reported. The higher one is the direct result of the quench, performed at fixed redshift (as is appropriate when simulating directly the equations of motion presented above). The lower value is for a annealing protocol whereby the redshift is released at the end of the main part of the simulation, either when the disclination network has filled the simulation box and rearrangements have come to a virtual standstill (this was done for $\tau = 0, \kappa = 2$) or when the disclination network first collides with its own periodic images (this was done for $\tau = 0, \kappa = 3$). This 'devil's advocate' annealing schedule finds the best possible free energy among states with topology close to the amorph, regardless of whether such states were dynamically accessible from the initial nucleus.

For $\kappa \leq 2$, the final redshift release makes no qualitative difference to the observed topology; moreover the free energies found after this procedure for ($\kappa = 2$) still lie above those of the ordered 'target' structure, as they do for all runs with $\kappa \leq 2$ done in the absence of a final redshift-release step. This confirms that the amorphous end-state is metastable, as claimed in the main text.

The quenches at $\tau = 0, \kappa = 3$ offer a test of Ostwald's rule of stages; for these parameters, the free energy of the final amorphous network (with or without redshift release, the latter in bold) lie further in free energy from the initial isotropic phase ($f = 0$) than the structure that was nucleated. When this is BPI, so do all remaining ordered phases. Thus the nucleus is now made of the phase whose free energy lies closest below that of the initial bulk; by Ostwald's rule, this should be the first phase to grow. Despite this, an amorphous network is formed, and the initial nucleus disappears – just as it did when the nucleated phase was the stable one. Therefore our results have no explanation in terms of Ostwald's rule; indeed, for this system, they disprove it.

In these high chirality runs, the final release of the redshift noticably changes the dynamics, accelerating the continuous ripening of the amorphous network towards the equilibrium O5 phase. No redshift release was performed for runs involving nuclei within a cholesteric matrix ($\tau = -0.5, \kappa = 1.2, 1.35$) due to the much longer simulation times required in this case. Indeed, for runs (F2,F3) the defect network did not fill the box by the end of the run and the quoted free energy densities in these cases are upper bounds. However, correcting for such volume-fraction effects shifts the values for the amorphs down by less than one percent, confirming their metastability.

The amorphous networks we report in this work appear closely related to BPIII, an equilibrium blue phase, believed to be amorphous, which is found experimentally at high chiralities. We address elsewhere (manuscript in preparation) the question of whether the chosen free energy density, Eq.2, can indeed predict a stable BPIII phase in that regime. Of significance here is the fact that it does predict a *metastable* BPIII phase for $\tau = 0$ and $\kappa = 2, 3$ (relevant to Figs.4,5, and S2). To establish this, we have created candidate BPIII structures by evolving an initial state consisting of randomly oriented and positioned double twist cylinders (DTCs), embedded in a cholesteric matrix. On suitable annealing (with redshift enabled), these relax to form amorphous networks, metastable relative to BPI/II, that on visual inspection look very similar to our end-state structures. However, for $\tau = 0, \kappa = 2, 3$, the DTC-based networks have a lower free energy ($\tilde{f} = 10^5 f = -3.104, -1.144$) than the amorphs formed in our nucleation runs with BPI/II. (Except for the case of the BPII-nucleated amorph at $\kappa = 3$, this remains true even if we violate the true dynamics by releasing the redshift.) Thus our end-state amorphs are *not* the disordered network phase of lowest free energy in any of these cases. Arguably however BPIII *is* that phase: certainly it must be so at higher chirality, where it is thermodynamically stable. Thus we do not designate our amorphs as belonging directly to a metastable branch of BPIII.

1. **D. Marenduzzo, E. Orlandini, M. E. Cates, J. M. Yeomans,** Steady-state hydrodynamic instabilities of active liquid crystals: Hybrid lattice Boltzmann simulations. **Phys. Rev. E 76, 031921 (2007).**
2. **O. Henrich, D. Marenduzzo, K. Stratford, M. E. Cates,** Domain growth in cholesteric blue phases: hybrid lattice Boltzmann simulations**. Comput. Math. Appl., doi:10.1016/j.camwa.2009.08.047[dx.doi.org] (2009).**
3. **M. E. Cates, O. Henrich, D. Marenduzzo, K. Stratford,** Lattice Boltzmann simulations of liquid crystalline fluids: active gels and blue phases. **Soft Matter 5, 3791-3800 (2009).**
4. **A. N. Beris, B. J. Edwards, Thermodynamics of Flowing Systems with Internal Microstructure (Oxford Univ. Press, New York, 1994).**
5. **P.-G. de Gennes, J. Prost, The Physics of Liquid Crystals (Oxford Univ. Press, New York, 1993).**
6. **K. Stratford, R. Adhikari, I. Pagonabarraga, J.-C. Desplat, M. E. Cates,** Colloidal jamming at interfaces: a route to fluid-bicontinuous gels. **Science 309, 2198-2201 (2005).**
7. **D. C. Wright, N. D. Mermin,** Crystalline liquids – the blue phases. **Rev. Mod. Phys. 61, 385-432 (1989).**
8. **C. Denniston, D. Marenduzzo, E. Orlandini, J. M. Yeomans,** Lattice Boltzmann algorithm for three-dimensional liquid-crystal hydrodynamics. **Philos. Trans. R. Soc. London, Ser. A 362, 1745-1754 (2004).**
9. **G. P. Alexander, J. M. Yeomans,** Stabilizing the blue phases. **Phys. Rev. E 74, 061706 (2006).**
10. **J. Englert, L. Longa, H. Stark, H. R. Trebin,** Fluctuations dominate the phase diagram of the chiral nematic liquid crystal**. Phys. Rev. Lett. 81, 1457-1460 (1998).**
11. **M. E. Cates, et al.** Simulating colloid hydrodynamics with lattice Boltzmann methods. **J. Phys. Condens. Matter 16, 3903 (2004).**
12. **R. Adhikari, K. Stratford, M. E. Cates, A. J. Wagner,** Fluctuating lattice Boltzmann. **Europhys. Lett. 71, 473-479 (2005).**

Supporting Table S1

Fig.	τ_{eq}	κ_{eq}	$A_{0,eq}$	γ_{eq}	τ	κ	A_0	γ	r	K	k_BT
2	0.75	2	0.0075	2.769	0	2	0.0069	3	0.91	0.02	0
3	-0.5	0.45	0.1295	3.176	-0.5	1.2	0.0182	3.176	0.83	0.01	0
4	-0.5	0.45	0.1295	3.176	-0.5	1.35	0.0144	3.176	0.83	0.01	0
S1	0.95	0.4	0.1918	2.714	0	2	0.0069	3	0.83	0.01	0
S2	-0.5	0.45	0.1295	3.176	-0.5	1.35	0.0144	3.176	0.83	0.01	8.33×10^{-6}
S3	0.95	0.4	0.1918	2.714	0	3	0.0031	3	0.83	0.01	0

Simulation parameters in lattice units: temperature τ_{eq}, chirality κ_{eq}, bulk free energy constant $A_{0,eq}$ and γ_{eq} at the equilibration point, temperature τ, chirality κ, bulk free energy constant A_0 and γ after the quench, redshift r as used during the equilibration and the main part of the simulation, elastic constant K, and noise temperature k_BT. For all runs the pitch $q_0 = \pi/16$; rotational diffusion constant $\Gamma = 0.3$; the tumbling parameter $\xi = 0.7$; the viscosity $\eta = 5/3$, and the fluid density $\rho = 2$.

Supporting Table S2

State	Fig.	τ	κ	r	$\tilde{f}(r)$	r'	$\tilde{f}(r')$
BPI-ISO-D	S4	0	2	0.83	-2.949	0.946	-3.066
BPII-ISO-D	2	0	2	0.91	-3.048	0.972	-3.088
CH	-	0	2	-	-	1.006	-0.826
BPI	-	0	2	-	-	0.846	-2.780
BPII	-	0	2	-	-	0.908	*-3.162*
O5	-	0	2	-	-	1.009	-3.048
BPI-ISO-D	S3	0	3	0.83	**-0.938**	0.949	-1.043
BPII-ISO-D	-	0	3	0.91	**-1.135**	0.959	-1.149
CH	-	0	3	-	-	1.006	0.003
BPI	-	0	3	-	-	0.921	-0.095
BPII	-	0	3	-	-	0.919	-1.063
O5	-	0	3	-	-	1.020	*-1.192*
BPI-CH-D	3	-0.5	1.2	0.83	-17.749	-	-
CH	-	-0.5	1.2	-	-	1.006	-16.466
BPI	-	-0.5	1.2	-	-	0.819	*-19.231*
BPII	-	-0.5	1.2	-	-	0.877	-18.973
O5	-	-0.5	1.2	-	-	0.952	-17.949
BPI-CH-R	4	-0.5	1.35	0.83	-13.580	-	-
BPI-CH-RN	S2	-0.5	1.35	0.83	-13.002	-	-
CH	-	-0.5	1.35	-	-	1.006	-11.825
BPI	-	-0.5	1.35	-	-	0.826	*-14.720*
BPII	-	-0.5	1.35	-	-	0.887	-14.615
O5	-	-0.5	1.35	-	-	0.969	-13.743

Free energy densities $\tilde{f}(r) \equiv 10^5 f(r)$ in LBU for the ordered blue phases (BPI, BPII and O5) and the cholesteric phase (CH) and for the amorphous networks grown from a BPI-droplet in isotropic (BPI-ISO-D) or cholesteric environment (BPI-CH-D), a BPII-droplet in isotropic environment (BPII-ISO-D) or from a BPI-rod in cholesteric environment with (BPI-CH-RN) and without noise (BPI-CH-R). The free energy density $f(r)$ of each phase was attained by direct evolution of the initial state at fixed redshift r; $f(r'), r'$ are corresponding values after redshift release. Numbers in bold provide tests of Ostwald's rule(see supplementary Text S1, section 6); italics identify the equilibrium phase at given τ, κ.

Supporting Figure S1

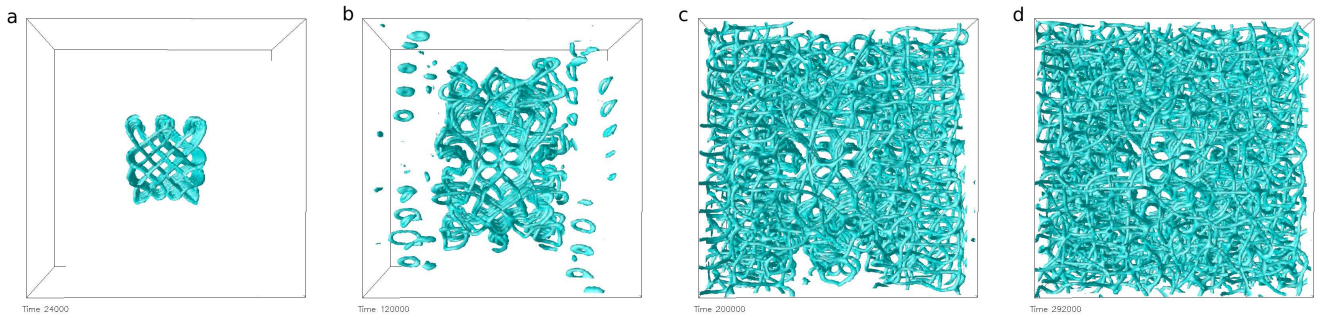

Fig. 1. [Fig.S1] Domain growth of a BPI rod in cholesteric environment including noise in the order parameter equation of motion. The noise strength was set to $k_BT = 8.33 \cdot 10^{-6}$ LBU. The pictures show isosurfaces of the order parameter at $t = 2.4 \times 10^4$ timesteps (a); $t = 1.2 \times 10^5$ (b); $t = 2 \times 10^5$ (c); and $t = 2.9 \times 10^5$ (d). The equilibration and quench were performed in exactly the same way as in the simulation of the BPI rod without noise (Figure 4 in main text). Note that from about $t = 10^5$ onwards, the disclination network ceases loses the symmetry of the initial state.

Supporting Figure S2

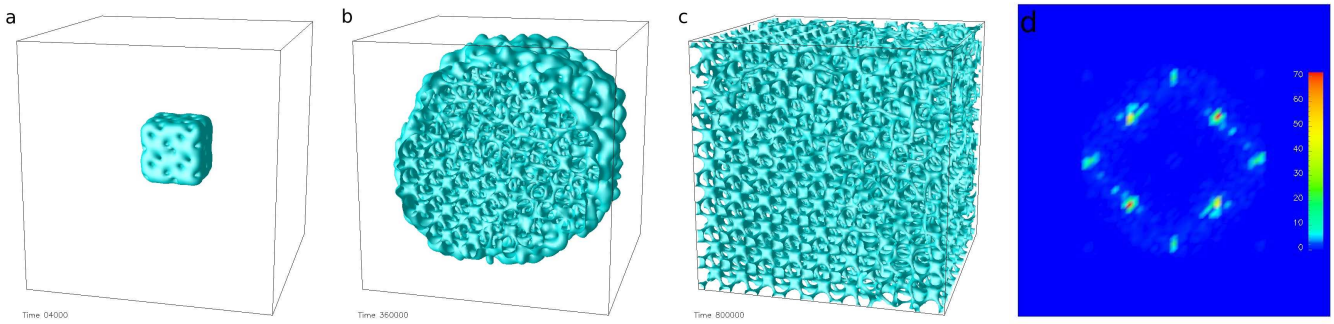

Fig. 2. [Fig.S2] Domain growth of a BPI droplet in isotropic environment at high chirality. The droplet was equilibrated near the isotropic-BPI boundary at $\tau = 0.95, \kappa = 0.4$ and then quenched to $\tau = 0, \kappa = 3$. At this point O5 is the thermodynamically stable phase. The pictures show the isosurface ($q = 0.12$) of the scalar order parameter during the equilibration (a), at an intermediate stage (b) and in the final state of the simulation (c). In (b) the isosurface has been cut at $y = 32$ to reveal the internal structure. In (d) a cut through the structure factor of the final state (c) along $k_z = 0$ for $k_x \leq k_y$ on the interval $[-\pi/2\ell, \pi/2\ell]$ is depicted. Although the Bragg-peak pattern appears rather blurred, the cubic signature of O5 is clearly recognizable.

Supporting Movies S1-S4

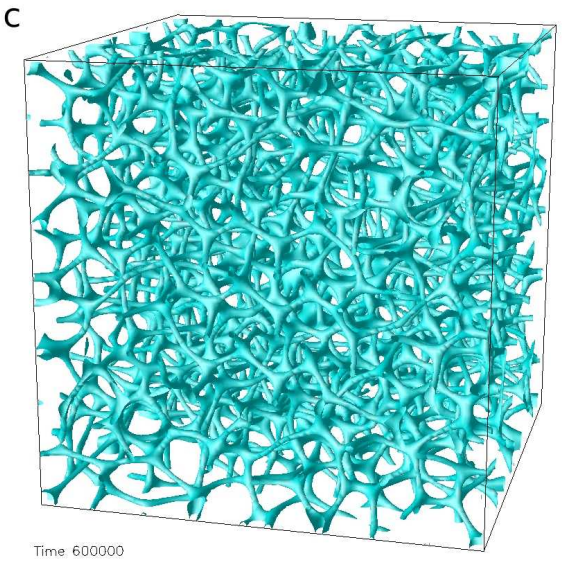

Fig. 3. [SM1.mov] Movie version of Fig. 2.

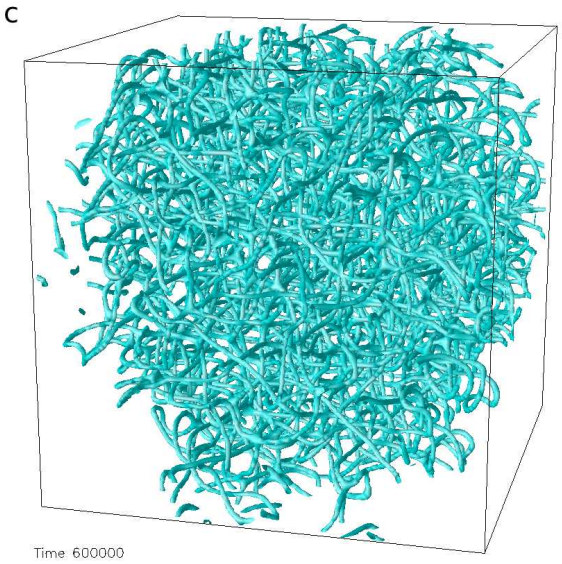

Fig. 4. [SM2.mov] Movie version of Fig. 3.

C

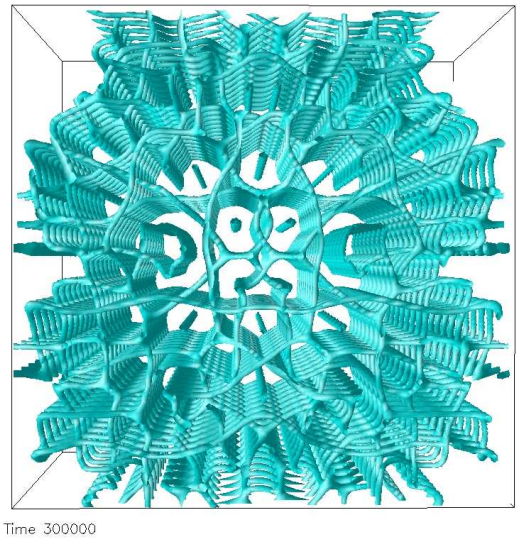

Fig. 5. [SM3.mov] Movie version of Fig. 4.

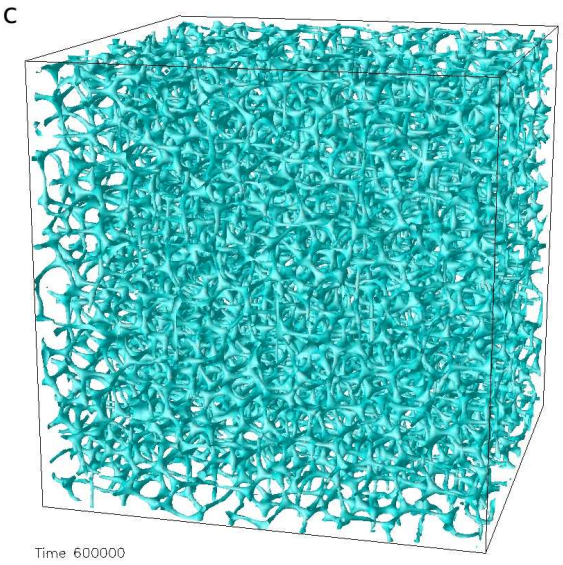

Fig. 6. [SM4.mov] Movie version of Fig. 5.